Research Article

Flexible and Dynamic Patch Reconstruction for Traveling Wave Magnetic Particle Imaging

Patrick Vogel* · Thomas Kampf · Martin A. Rückert · Volker C. Behr

Department of Experimental Physics 5 (Biophysics), University of Würzburg, Würzburg, Germany
*Corresponding author, email: patrick.vogel@physik.uni-wuerzburg.de

Abstract

Different types of scanners have been presented since the first publication of Magnetic Particle Imaging (MPI) in 2005. As a result, there are different types of reconstruction methods available, which can be separated into two basic concepts: reconstruction using a system matrix and reconstruction using a direct deconvolution. Both methods have their merits and drawbacks. For the first approach hardware parameters like sampling rate and frequencies have to be chosen carefully to fit the parameter selection process required for the system matrix. For the other approach the temporal and spatial homogeneity of the magnetic field gradient over the entire FOV has to be high to perform an accurate reconstruction, which results in smaller FOVs. This paper presents a novel reconstruction method, which combines the advantages of both aforementioned methods to be more flexible during the entire reconstruction process. Furthermore, it enables the possibility of performing a dynamic patch reconstruction, which allows selecting arbitrary areas of the FOV for higher resolution reducing reconstruction time significantly. In addition, this new reconstruction improves the image quality of a Traveling Wave MPI scanner substantially.

I. Introduction

Since the first publication of Magnetic Particle Imaging (MPI) [1] several different scanner types were published [2]. For each scanner type a reconstruction process is available, which takes into account the scanning type, field-free point (FFP) [1] or field-free line (FFL) [3], and the scanning mode, trajectory of the FFP or projection of the FFL. Basically, there are two different kinds of reconstruction processes: the system matrix reconstruction (SMR) [4] and the deconvolution reconstruction (DeR) [5–7].

The DeR approach contains several steps: after the acquisition of the signal, in a first step the distortion caused by the receive chain has to be corrected before the data are gridded to get a 1D or 2D raw-image. Finally, this raw-image is reconstructed using a deconvolution algorithm and corresponding kernel [6].

The SMR approach works with a transformation matrix, which transforms the spatial distribution of the magnetic nanoparticles into the corresponding signal acquired with the very system the matrix is designed for. This matrix can be measured point-by-point acquiring the signals of a delta-like sample, which is positioned inside the FOV using a robot. This approach is very time consuming but results in a transformation, which contains all signal transformations as well as hardware distortions. Every dataset is run through a Fourier transformation before a set of peaks are chosen, which are used in the system matrix as encoding parameters. Finally, the reconstruction of the image can be performed by solving

the inversion of the system matrix [4].

However, both basic methods come up with some constraints: the SMR requires a specific choice of hardware parameters like the sampling rate, the excitation frequencies and the trigger point of the signal acquisition. The reason is the peak-picking process for building the system matrix. To avoid Fourier-leakage[1] it is necessary to choose these parameters carefully [8].

In addition, the trigger point has to be determined precisely, because of phase errors that cause the reconstruction to fail. This results in an inflexible hardware setup, which has to be adapted to these parameters.

On the other side, the DeR does not have this restriction. The reason is the gridding step, which decouples the reconstruction process from the hardware. The sampling rate, excitation frequencies and trigger point are freely selectable. However, the drawback of the deconvolution reconstruction is its sensitivity to trajectory distortions caused by magnetic field inhomogeneities created by the scanner hardware. Using a single deconvolution kernel for the entire raw-image yields geometrically distorted images and signal fluctuations. These issues can be solved by using highly accurate magnetic fields and smaller FOVs to ensure a uniform trajectory of the FFP.
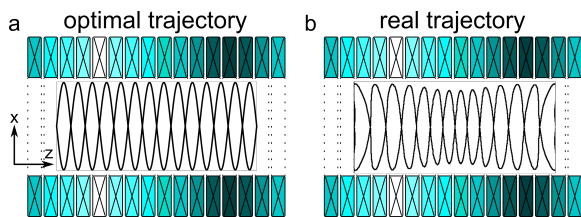

Figure 1: Sketch of the dynamic linear gradient array (dLGA) of a TWMPI scanner running in slice-scanning mode (SSM). The black sinusoidal pattern indicates the trajectory of the FFP traveling through the FOV, where (a) shows the optimal trajectory and (b) shows the real trajectory. The real trajectory is the result of a simulation of the real TWMPI scanner with the frequencies $f_1 = 1\,\text{kHz}$ and $f_2 = 16\,\text{kHz}$.

The traveling wave MPI scanner is an alternative scanner design, which uses a dynamic linear gradient array (dLGA) for the generation of a FFP with a strong gradient traveling along the symmetry axis. Additional saddle-coils, which are oriented orthogonally to the dLGA, are used for moving the FFP arbitrarily through the FOV and scanning an entire 3D volume with different trajectories. A receive coil parallel to the dLGA is used for signal acquisition [6, 9–11].

Because of the small hardware dimensions in contrast to the size of the FOV, this scanner type comes up with

a distorted magnetic field, which results in an irregular trajectory of the FFP (see Fig. 1)[2].

In previous publications a 2D deconvolution method (DeR) followed by an additional morphing algorithm, which corrects the distortions in a post-processing step, were used for the image reconstruction [6, 9].

However, this correction step still shows geometry distortions for reconstructing more complex samples (see Fig. 2).
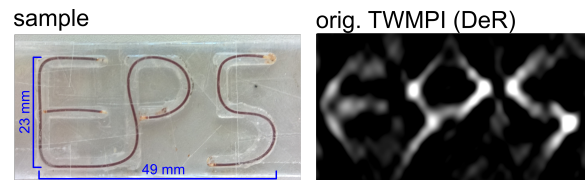

Figure 2: Reconstruction of the measured EP5 logo using the deconvolution approach (DeR). The phantom consists of a plastic tube (inner diameter of 0.5 mm) filled with undiluted Resovist® (Bayer, Germany).

This paper presents a novel reconstruction, which combines parts of both reconstruction methods to overcome the issues of geometry distortion caused by the DeR and the inflexibility of the SMR.

II. Methods

In Fig. 3 a flow chart is presented to give an overview of the different reconstruction methods. The new reconstruction approach is a hybrid method, which combines the system matrix with the flexibility of the DeR.

The basic part of the proposed reconstruction is a system matrix approach, which either uses measurement-based datasets [4] or model-based datasets [12]. Once the system matrix has been obtained a Tikhonov regularization algorithm or singular value decomposition (SVD) algorithm can be used for the matrix inversion required for image reconstruction [8, 13, 14].

The reconstruction process used in this manuscript contains of three major steps:

1. Building the system matrix M

2. Performing a truncated SVD on M

3. Calculating the pseudo inverse $\tilde{M}^{-1}$.

The system matrix M can be seen as the transfer function between the measured data vector (image) u and the source point distribution vector (distribution) c:

$$M c = u \qquad (1)$$

$$c = M^{-1} u. \qquad (2)$$

---

[1] Fourier-leakage or Fourier-bleeding: Performing a Fourier transformation of a discrete dataset results in a spectrum convolved by a sinc. The energy will bleed over adjacent bins instead of being in a specific bin. A similar effect is caused by the non-integer ratios of sampling rate and frequencies.

[2] The chosen frequencies f_1 and f_2 for driving a TWMPI system in slice-scanning mode (SSM) follow the rule to cover within one period of f_1 a optimally dense trajectory while the frequencies stay in the range below 20 kHz, which allows using common audio amplifiers.
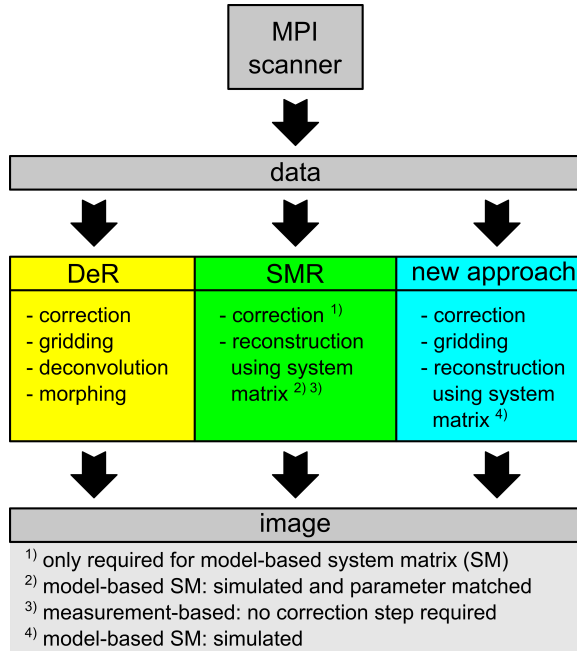
Figure 3: Flowchart of the different reconstruction methods showing the basic steps required to reconstruct the final images.

To get the real distribution c the inverse of the system matrix M^{-1} has to be calculated. A robust and flexible method to solve such an ill-posed problem and determine M^{-1} is the SVD. For that the singular value decomposition of the matrix $M \in \mathbb{R}^{m \times n}$ is calculated:

$$M = U W V^{\mathrm{T}}, \tag{3}$$

$$U \in \mathbb{R}^{m \times m}, \quad V \in \mathbb{R}^{n \times n}, \quad W = \mathrm{diag}(k_1, \dots, k_n) \in \mathbb{R}^{m \times n}.$$

These matrices can be used to determine the Moore-Penrose pseudo inverse $\tilde{M}^{-1}$, which is a generalization of M^{-1} and solves the reconstruction problem in a least square sense

$$\tilde{M}^{-1} = V W^{-1} U^{\mathrm{T}}. \tag{4}$$

With the pseudo inverse $\tilde{M}^{-1}$ the distribution c is calculated.

In the last step it is possible to optimize the reconstruction by truncating the eigenvalues k_{trunc} and applying a suitable filter to weight the eigenvalues [15, 16].

The amount of parameters used for modeling the system matrix is limited by the robustness of the inversion algorithm and hardware limitations (RAM and CPU power). The system matrix can be built using different approaches.

II.I. Fourier-Based System Matrix

The first approach follows a similar pattern to the system matrix approach using model-based datasets [8]. For a TWMPI scanner, which uses a different trajectory [9], the

proposed peak-picking process [8] in the Fourier spectrum cannot be applied in this form on the TWMPI data, because the trajectories follow different schemes [4]. In the case of a TWMPI scanner using the rotational slice-scanning mode (rSSM) [10] for scanning an entire 3D volume, the Fourier spectrum of the signal shows multiple combinations of higher harmonics and side bands of the excitation frequencies f_1 and f_2 ($f_1 < f_2$). The position of the harmonics is given by the following scheme:

$$k_{i_1, i_2} = \begin{cases} i_2 f_2 + 2 i_1 f_1 & \text{, if } i_2 = \text{odd} \\ i_2 f_2 + \big(2 i_1 - \mathrm{sign}(i_2)\big) f_1 & \text{, if } i_2 = \text{even} \end{cases}, \tag{5}$$

$$i_1 \in \mathbb{Z} \backslash \{0\}, \quad i_2 \in \mathbb{N}.$$

In Fig. 4 the table shows a small selection of the system functions corresponding to their calculated harmonics in the spectrum. These images are based on the real part of the signal and describe the encoding pattern (system functions) for the reconstruction process. With increasing parameters and the pattern shows finer structures, which demonstrate the encoding capacity. The real and imaginary parts show different patterns, which increase the number of encoding parameters available for the system matrix.
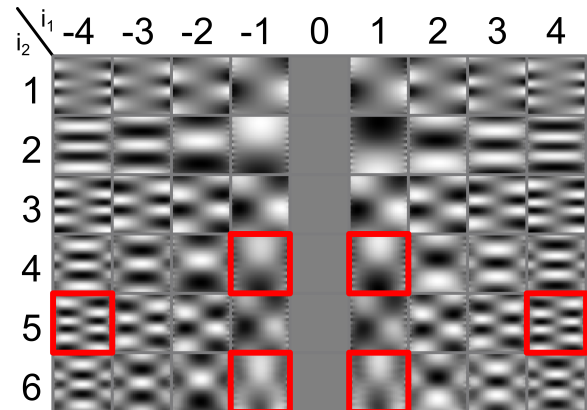

Figure 4: Table of system functions based on a model-based simulation of a TWMPI scanner. The different patterns give an idea of the encoding process, which improves with the use of more harmonics. The indicated areas (red rectangles) show the problematic patterns, which are the result of Fourier-leakage.

The pattern images are based on a model-based dataset created with a home-built software tool, which can simulate the real TWMPI scanner [6, 9, 17]. The sampling rate is set to 100 MS/s and the excitation frequencies are $f_1 = 919$ Hz and $f_2 = 16123$ Hz. The frequencies are based on the hardware of the TWMPI scanner: after tuning and matching the coils, the exact eigenfrequency of the system is determined. The sampling rate up to 100 MS/s is chosen for a lower noise level.

However, as mentioned this approach comes with the issue that a specific sampling rate and frequency ratio

is required to avoid Fourier-leakage. In addition, the trigger point for data and system matrix datasets should be identical. In Fig. 4 the issue related to Fourier-leakage can be seen: for odd i_2 the patterns are the same for $i_1 = -i_1$. For even i_2 the patterns should be inverted. The red areas indicate the problematic patterns, which do not show the expected behavior on both sides (see Sec. A).

To overcome this issue the time signal has to be resampled to avoid Fourier-leakage. There are different approaches available, which can be used for the resampling process [18].

Because of the identical patterns in the side bands (using the appropriate sign), only one part of the side band can be used for building the system matrix in order to avoid ambiguities. This causes a decrease in available number of parameters.

Therefore, only the right side of the harmonic band is used and real and imaginary parts have to be considered to build the system matrix. The reason is that the encoding in z-direction is a pure encoding by phase (see Sec. A) [9]. The picking process follows the formula:

$$I_{i_1,i_2} = \left\lfloor \left(i_2 f_2 + (2i_1 - ((i_2 + 1) \bmod 2)) f_1 \right) \frac{l_{\text{data}}}{SR} + 0.5 \right\rfloor, \quad (6)$$

$$i_1 \in \mathbb{N}, \quad i_2 \in \mathbb{N}\setminus\{1\},$$

where I_{i_1,i_2} denotes the index in the Fourier transformed dataset with the length l_{data} and the sampling rate SR. It has to be emphasized that in this case the peak picking process starts at $i_2 = 2$ at first because of the hardware filtering (Chebychev high pass filter at 20 kHz) in the real system.

For an initial test a system matrix with a size of 1932×1891 entries $((2 \times 21 \times 46) \times (31 \times 61))$ is built with the values $i_1 = 1, \ldots, 21$ and $i_2 = 2, \ldots, 47$ and a factor of 2 for real and imaginary parts.

In Fig. 5 the reconstruction results are shown for different values of k_{trunc}. With increasing k_{trunc} the image quality increases but at the same time the stability of the reconstruction process suffers. Moreover, even a small variation of the trigger point of only $1/SR = 100$ ns ($SR = 1 \cdot 10^7$ 1/s) results in a massive decreasing of the image quality.

In the following, an additional gridding step, known from the DeR approach [11], is used before the parameter selection to circumvent the resampling process[3] and the issue with the trigger point. This step decouples the hardware and its parameters from the following reconstruction process.
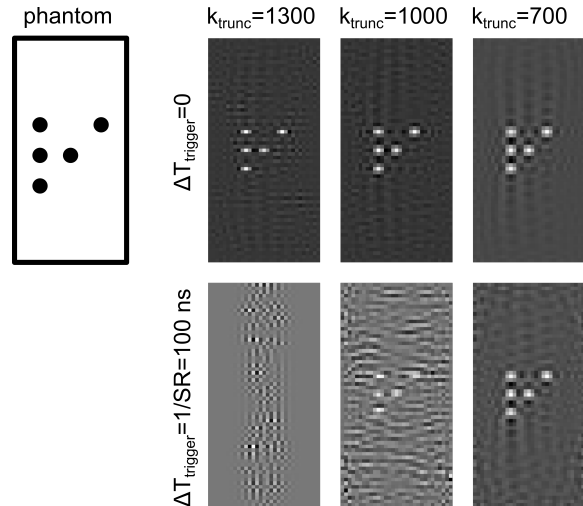
Figure 5: Reconstruction using a Fourier-based system matrix of a simulated phantom with different k_{trunc} values and trigger points. Even small variations of the trigger point result in a massive deterioration of the image.

II.II. Image-Based System Matrix

In contrast to the SMR using a measurement-based system matrix the simulation-based system matrix approach requires a correction of the receive chain. This has to be done after digitizing the acquired data before the gridding process, because of the amplitude and phase distortions caused by individual components in the receive chain like filters and pre-amplifiers (see Fig. 3). The corrected signals are gridded point-by-point on a 2D image according to the excitation frequencies used for scanning [6, 11]. This gridding step mitigates the Fourier-leakage arising from the frequency and sampling rate ratio. Because of the high sampling rate (100 MS/s) and the selection of a huge 2D image the mismatching of data points and associated pixels is very small. It also solves the issue with the trigger point described in Sec. II.I. After this step all raw-images represent a 'normalized' signal regardless of the origin of the data (TWMPI scanner with different settings or simulated datasets [17]). Thus, the final raw-image is independent of the hardware and the consecutive reconstruction process.

In Fig. 6 on the left a raw-image of a point-sample is shown displaying the point-spread-function[4] (PSF) of the system at this specific position (here in the center of the FOV) [4]. The raw-image varies slightly when moving the sample step-by-step through the entire FOV. In the end a set of n raw-images with a size of m, one for each position, is available, which represent a point-by-point transformation of the entire scanner system.

The image-based approach now directly uses the 24

---

[3]A gridding process cannot completely overcome issues such as Fourier-leakage. Gridding a data set point-by-point on a discrete surface also requires rounding operations. However, the effect is much smaller especially at very large surfaces.

[4]A TWMPI scanner provides two different shaped PSFs depending on the alignment of the receive coil [9, 10]. Here the PSF for a receive coil aligned into the z-direction (parallel to the dLGA) is shown.
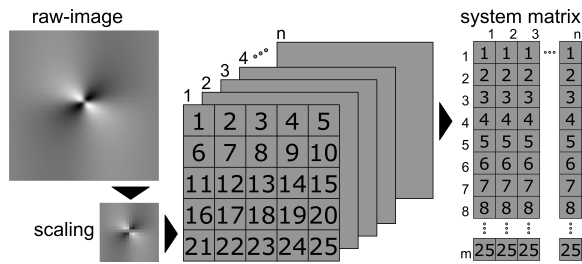
Figure 6: Building an image-based system matrix: as first step the corrected raw-image is scaled down. After that every pixel value is directly transferred to the system matrix with n labelling the positions of the sample used for measurement or calculation of the PSF and m is the number of points in space, where the PSF was calculated.

Figure 7: After a 2D Fourier transformation the spectrum contains most of the signal information in the center. This compact signal can be directly used for filling up the system matrix.

bit[5] gray-scaled pixel values of the raw-image column-by-column as encoding parameters, which are filled row-wise into the system matrix (see Fig. 6).

Because of the highly resolved raw-images (up to $500\,\text{px} \times 500\,\text{px}$) the amount of pixels is extremely high. This is useful to reduce gridding artifacts caused by the choice of hardware parameters and mismatching of spatial data points to pixels due to rounding errors. To avoid a huge system matrix, which results in long calculation times, the raw-images have to be scaled down prior to creating the system matrix.

II.III. Fourier-Scaled Image-Based System Matrix

The scaling process used in the image-based system matrix to reduce the amount of data can lead to information loss. This means decreasing the number of pixels in a picture results in a reduction of information by averaging pixel information. It is the same effect as using a cut-off in the spectrum, which results in a loss of resolution. To reduce this effect in Fig. 7 a view of a 2D Fourier spectrum of a raw-image is shown with most signal located in the center corresponding to low frequencies.

According to Fig. 6 for the Fourier-based system matrix approach the complex values from the center of the 2D spectrum are pixel-wise filled in the system matrix. This direct data processing reduces information loss (here of lower frequencies) arising from the image scaling process while yielding the same size of the system matrix. It is important that only half of the spectrum must be used because of redundant information in the spectrum. This approach is quite similar to the peak-picking process described in Sec. II.I but with the additional gridding step.

It is also possible to reduce the resolution of the raw-image by symmetrically cropping the 2D Fourier spectrum (Fig. 7). After an inverse 2D FFT a size-reduced raw-image is obtained, which can be processed in the same way as the image-based approach described in Sec. II.II Because of the cropping in Fourier space the information loss during the scaling process is different from the direct scaling process (see Sec. B).

II.IV. Patch Reconstruction

In the last sections, ways to decouple the hardware from the parameter-picking process for generating a system matrix were presented. However, one issue remains to be solved: for obtaining higher resolution the amount of parameters has to be increased to encode the desired FOV. Increasing the size of the system matrix results in a more time consuming inversion process using an SVD algorithm. Of the presented approaches, the faster weighted Tikhonov algorithm cannot be used because of the unknown weighting of the eigenvalues, which is required for filtering [14]. The spatial localization of the PSF (see Fig. 7) combined with the image-based system matrix (Sec. II.II) offers an option to avoid this issue. Using this technique for building the system matrix allows defining arbitrary areas on the image that can be reconstructed separately. The selection of specific areas for the reconstruction results in a significant reduction of computing time. Furthermore, it even allows selecting areas that will be reconstructed with a higher resolved system matrix yielding higher resolved parts of the image. In Tab. 1 an overview of system matrix sizes and the complexity[6] of the SVD calculation are given, which causes increased computing times at higher resolutions [19].

Initially, for a new reconstruction process, a lowly resolved grid is used to create an overview of the image in a short time (lowly resolved image) (see Fig. 8: raw-image → grid 1). After that, the user has the option of choosing arbitrary areas to be reconstructed with higher resolution (see Fig. 8: gridding steps). While the first step only uses a small-sized matrix for the entire image in the second step a much smaller area is reconstructed using the resolution and input datasets of a more highly resolved grid. This

---

[5]The ADC works with 12 bit. After digitization it is necessary to make some corrections such as calculating the distortions of the receive chain and filtering in Fourier space [11]. Thus, it is useful to work with a higher precision on the values to avoid introducing numerical errors.
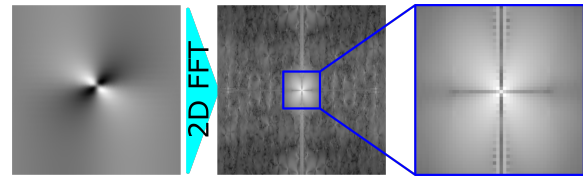
[6]The complexity of a standard SVD implementation (alglib.net library) is given by $O_{\text{SVD}} = \min\left(nm^2, n^2m\right)$.

Table 1: Increasing the size of the system matrix results in a massively growing complexity.

grid-size ($n \times m$)	size factor	SVD complexity
$(17 \cdot 25) \times 1275$	147.5	$2.3 \cdot 10^{11}$
$(9 \cdot 13) \times 351$	11.0	$4.8 \cdot 10^{6}$
$(5 \cdot 7) \times 105$	1.0	$1.3 \cdot 10^{5}$

process can be iterated several times. Furthermore, in later steps it is possible to reconstruct specific separated areas using the patch reconstruction method to enable highly resolved images without increasing the size of the system matrix making it more practical working on huge datasets. Reconstructing only specific areas using the proposed selected patch reconstruction (SPR) approach results in a faster reconstruction process by reducing the matrix size.
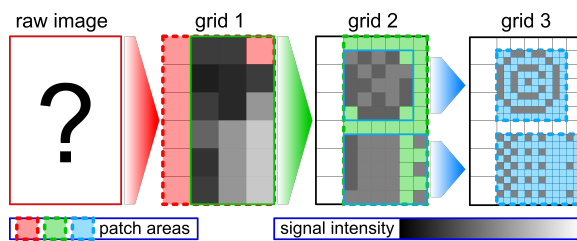
Figure 8: After a 2D Fourier transformation the spectrum contains most of the signal information in the center. This compact signal can be directly used for filling up the system matrix.

III. Results

All following images were reconstructed using a model-based system matrix, which was generated in a virtual TWMPI scanner by simulating the input dataset point-by-point [4, 17]. The maximal size of a coronal 2D imaging plane is 121×241 points. This is the highest available grid for the reconstruction representing a grid with a resolution in a real TWMPI system of $250\,\mu m$ [6, 9]. This covers a FOV with a width of $30.25\,mm$ and a length of $60.25\,mm$. With a gradient strength of about $4\,T/m$ (z-direction) a resolution of $1\text{-}1.5\,mm$ (z-direction) and $2\text{-}3\,mm$ (x-, y-direction) is achievable using Resovist$^{\circledR}$ (Bayer, Germany) [4, 10, 11, 18]. This results in an up to four times oversampled system matrix in relation to the resolution capability of the scanner, which is required to suppress partial volume and localization errors in the reconstructed image.

Firstly, every dataset is gridded on a 2D surface with a size of $500\,px \times 500\,px$ resulting in a total size of all input datasets of about 45 GB. These data act as starting basis for building the system matrices required in later reconstruction steps. Depending on the desired resolu-

tion, the grid is chosen and the size of the raw-image is adjusted. This follows the rule that the number of input-data m (parameters required for the reconstruction) has to be greater than the output-data n (number of pixels of the reconstructed image) to get an overdetermined set of equations.

The complexity of a completely filled matrix using all parameters with a matrix size of 250000×29161 is $2.1 \cdot 10^{14}$. This would result in a computation time of about 85 days on a current fast CPU (single thread) and require about 500 GB RAM for the inversion. The system matrix itself would have a final size of about 57 GB[7].

III.I. Image-Based vs. Fourier-Scaled Image-Based

The first results show the reconstructed images using the image-based approach described in Sec. II.II in contrast to the Fourier-scaled image-based method (Sec. II.III). In Fig. 9 the identical measured raw-data of a EP5-sample (see Fig. 8) is used with either reconstruction processes.
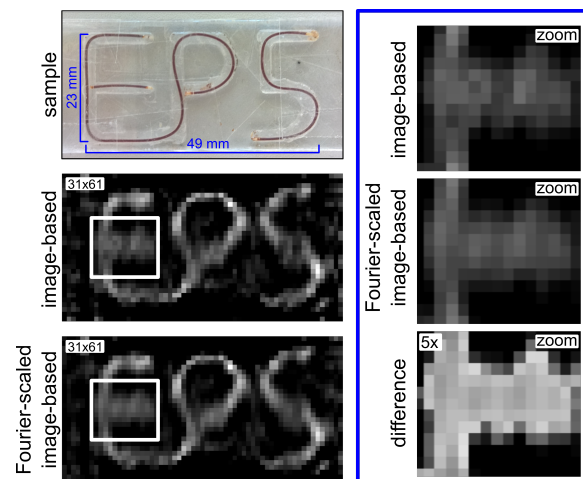
Figure 9: Comparison of the reconstruction methods: image-based and Fourier-scaled image-based reconstruction of a measured EP5-sample. The image quality is comparable. A zoom into a specific area compares the different scaling processes showing a slight smoothing effect of the Fourier-scaled reconstruction. The intensity of the difference image is scaled by a factor of 5.

In both cases the reconstruction grid was 31×61 and the size of the input images of 50×50 pixels (down scaling factor of 10) corresponding to system matrices of 2500×1891. Both reconstructions have comparable image quality and show a significant improvement in contrast over the DeR result shown in Fig. 2. The additional zoom-in pictures (Fig. 9) show only small differences between both reconstructed images, which are the result

---

[7]These values are based on an extrapolation calculation on a matrix with 10000×2000 entries, which requires about 10 minutes running single threaded on a current fast CPU.

of the different system matrices and their properties (see Sec. B).

III.II. Selected Patch Reconstruction

Fig. 10 shows the reconstruction process using the selected patch reconstruction (SPR) described in Sec. II.IV on a simulated dataset of a grid of dots with different distances (Fig. 10 (a)). In a first step, a reconstruction of the full image is performed at a low resolution (grid size of 16×31 and image size of 30×50 pixels) (Fig. 10 (b)). The computation time for the entire process is 21.4 seconds (17 seconds for the image preparation and 4.4 seconds for the SVD). The reconstructed image provides an overview of the entire FOV with the dots on top and in the center being clearly separable. The dots in the lower section cannot be resolved. Dots not matching the exact location of grid points result in slight distortions in their representation in the image.
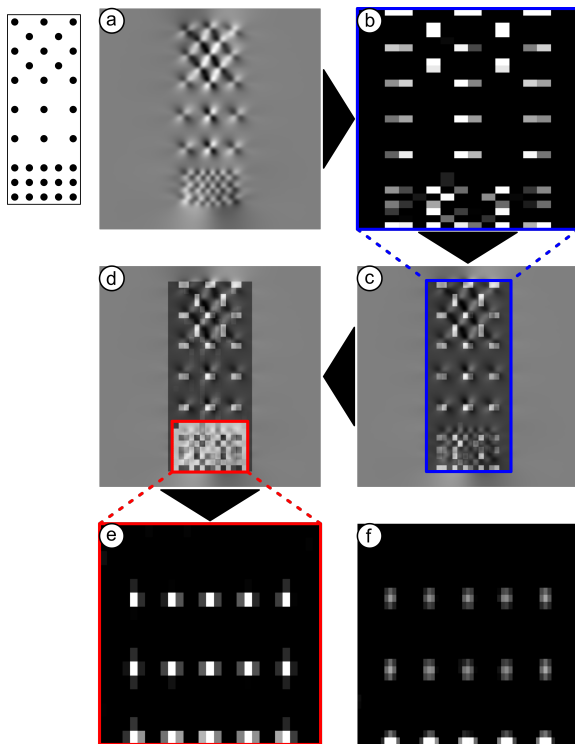

Figure 10: Reconstruction process using the selected patch reconstruction (SPR) demonstrated on a simulated dataset: (a) Raw-image of a simulated dataset containing dots in different patterns. (b) First reconstructed image with a low resolution (grid size 16×31). (c) In the next step this image has to be co-registered with the original raw-image to ensure the correct pixel-picking for the following reconstruction steps. (d) The red frame indicates the selected area, which will be reconstructed with a higher resolution. (e) Reconstruction of the selected area (patch grid size 29×31) at a higher resolution (2 times higher). (f) The same area with a higher resolved grid (patch grid size 57×31) (4 times higher).

In the following, this reconstructed low resolution-image has to be co-registered with the original raw-image (Fig. 10 (c)). This registration step is necessary to ensure covering the right area on the raw-image and selecting the correct data (pixels) from the raw-image for the next reconstruction step. This has to be done only once for each new dataset and hardware setting to set the scaling parameters. In the next step, the user can choose an arbitrary area (red rectangle) from the raw-image to be reconstructed at a higher resolution (Fig. 10 (d)). The reconstruction process now works on the next higher resolved grid with a computation time of about 20 seconds for a matrix of 2035×464 representing the selected area (patch grid size of 29×16 and raw-image size of 55×37 pixels). The dots now are clearly distinguishable. Fig. 10 (f) shows the same area with an even higher resolution, which has a computation time of about 85 seconds for a matrix with 2035×1767 (patch grid size of 57×31 and raw-image size of 55×37 pixels). The apparent increase of the signal intensity for points on the bottom edge of the image is caused by signal from outside the selected area, which is projected onto the border of the image [20] (see Sec. C).

III.III. SPR on Real Data

Fig. 11 shows the SPR approach on a measured dataset. The dataset was acquired with a high-resolution TWMPI scanner described in [21]. This scanner has an FOV of 44 mm in length and 23 mm in diameter and works with a gradient strength up to 7.5 T/m. Because of the identical hardware proportions, it is possible to use the same model-based input dataset for the entire reconstruction process. The only difference is the grid resolution, which is in the case of the smaller TWMPI scanner about 150μm.

The measured phantom contains six tubes filled with LS-008 (Lodespin Labs, USA), which are orientated orthogonally to the scanning slice. The tubes have an inner diameter of 1 mm and are spaced 0.5 mm, 1 mm and 1.5 mm. The first image shows the low-resolution reconstruction of the sample, the second the reconstructed area at a higher resolution. The third image shows the same area at an even higher resolution and the forth the highest possible resolution[8]. This image shows clearly the separation of the tubes with a distance of 0.5 mm. It also demonstrates the effect of projected signal from outside the selected area, which results in bifurcation artifacts [20]. The sample appears distorted in the fourth image because the horizontal axis is scaled by a factor of 4 for better visibility. In the second row, the tubes are reconstructed pairwise at the highest grid resolution. The imaging artifacts of the highest resolved image in the up-

---

[8]The highest possible resolution depends on the accuracy of the model-based datasets. It is reasonable to use the theoretical resolution of the MPI scanner as a reference to avoid unnecessary amounts of data.

per row are not present in this reconstruction because the structure of interest is completely placed inside a single patch. Only in the very corners projected signal from outside is visible, which can be clearly separated from samples.
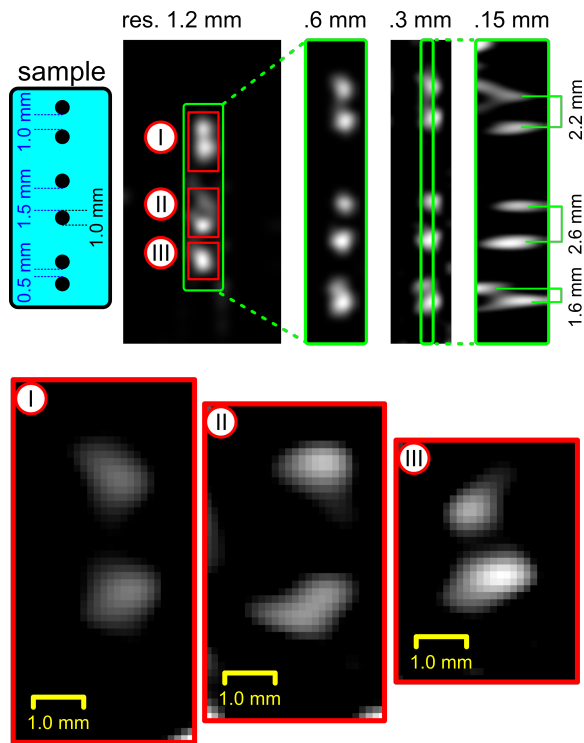

Figure 11: Reconstruction process using patch reconstruction on a measured dataset (μTWMPI scanner with a gradient strength of 7.5 T/m and a FOV of 44 mm in length and 23 mm in diameter): Starting with a lowly resolved image (top left) the following images show higher resolved images from the selected areas (indicated by the green rectangles). Please note the changed aspect ratio from the third to the fourth image. The images (I-III) show the separately reconstructed areas on the highest resolution (grid resolution 0.15 mm).

IV. Discussion

The proposed patch reconstruction method allows to reconstruct specific areas of the image because of the spatial localization of the PSF (Fig. 7). However, signal of a sample, which is located just outside the selected area, can create artifacts appearing as projections onto the border of the reconstructed image (see Fig. 7 (f) and Fig. 11). This effect can be suppressed by cropping the image by one pixel on all sides [20].

Furthermore, there is another approach, which could reduce the influence of the projected signals. This approach uses additional input datasets with a coarser gridding outside the selected area for building the system matrix. This increases the size of the system matrix

marginally, but can result in a more accurate reconstruction in the selected area, because signal from outside the selected area is processed separately and will not be projected onto the borders. The selection of further datasets outside the selected area can be implemented in the form of a dynamic selected patch reconstruction (dSPR) using a dynamic multigrid approach (e.g. Voronoi gridding [22]). However, this approach raises some new challenges such as a suitable implementation of a multigrid algorithm allowing to build a grid with a variable granulation or a robust algorithm for picking the pixels from the raw-images. Working on the SPR is less complex, because the selected area yields the pixel dimensions on the raw-image, but in the case of dSPR this selection process is not straight-forward because of the variable grid size. This could be avoided by setting the size of the pixels to maximum value, but at the cost of a growing system matrix and long computation times.

The proposed reconstruction methods as well as the different approaches for filling up the system matrix are in a very early state of investigation. Therefore, the influence of the different system matrices on reconstructed images and desired properties of (TW)MPI systems have to be further examined in more detail.

V. Conclusion

This paper presents a flexible reconstruction process based on the system matrix approach, which offers a much better image quality in contrast to a direct deconvolution reconstruction method using a 2D deconvolution. This approach overcomes the geometry distortions in TWMPI caused by temporal and spatial inhomogeneities of the magnetic field gradient over the FOV. It also decouples the hardware and its settings from the following reconstruction process by using a gridding step to generate 'normalized' raw-images. This results in high flexibility for the use of identical model-based datasets for different TWMPI scanner sizes (e.g. TWMPI vs. μTWMPI) and for settings (e.g. arbitrary excitation frequencies, sampling rate and trigger point). This makes the method very versatile.

Furthermore, several ways of filling the system matrix are introduced. Instead of Fourier-based data image-based data are used for this step, also motivating the selection patch reconstruction (SPR). The SPR offers the capability of working on very large datasets. It reduces the computation time for highly resolved images by calculating only arbitrarily selected areas of interest reducing the data for the reconstruction. This makes this method practicable for reconstruction of large datasets to obtain higher resolved images in a shorter time.

VI. Acknowledgments

A. TWMPI System Function Patterns

In Fig. A.1 an overview of the system functions of a Traveling Wave MPI scanner is given. For building a system matrix the real and imaginary parts have to be taken separately. The reason is pure encoding by phase in the z-direction (vertical in the 2D image) [9], which cause the absolute values of the pattern not to exhibit any vertical structures for increasing i_2. Only in the real and imaginary value pattern this structure can be seen.
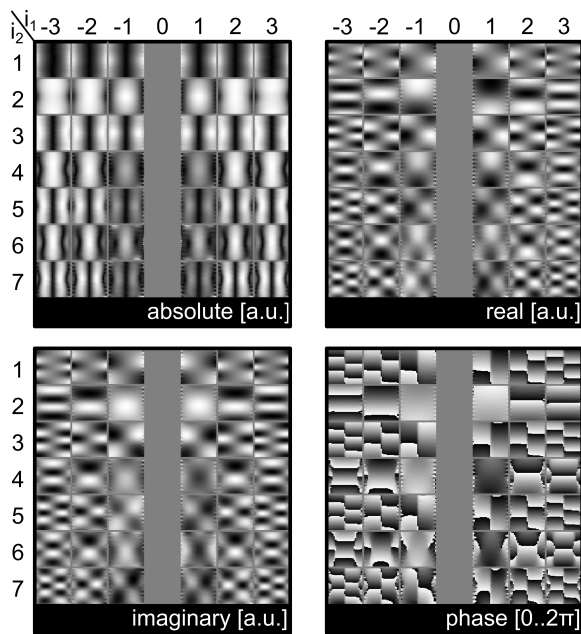

Figure A.1: An overview of the first system functions of a TWMPI scanner. The absolute, real, imaginary and phase value pattern are shown.

In Fig. A.2 a more detailed view on the effect of Fourier-leakage is shown. As an example the values for two pairs of system functions are given: the calculated frequency f_{i_1,i_2} and the corresponding index I_{i_1,i_2} (rounded value and exact value) based on the real excitation frequencies of the TWMPI scanner ($f_1 = 919$ Hz and $f_2 = 16823$ Hz).

The index can be calculated using the following formula:

$$I_{i_1,i_2} = k_{i_1,i_2}/SR \cdot l_{\text{data}} \quad (A.1)$$

whereby k_{i_1,i_2} means the frequency of the harmonic (see Sec. II.I), SR is the sampling rate and l_{data} the length of the dataset (in the case of $SR = 100$ MS/s and an acquisition time of 20 ms the data length is $l_{\text{data}} = 1 \cdot 10^6$).

In the case of pair (II) both index values are close enough to an integer value, which is unproblematic. In the case of pair (I) one of the indices lies between two integer values. Due to rounding issues, this can result in picking the false pattern, which has a major impact because of the almost inverted patterns for adjacent indices.
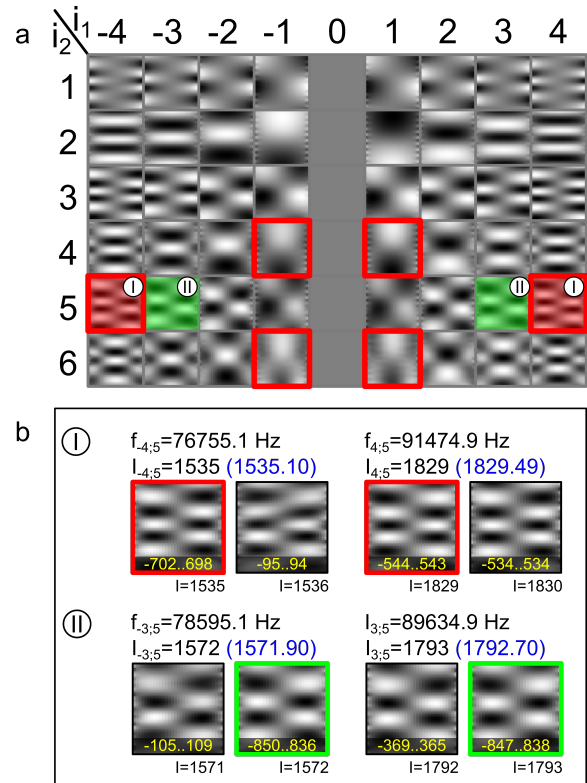

Figure A.2: (a) An overview of the system functions (real part). The red rectangles indicate the pairs, which show an unexpected behavior. (b) Two representing pairs are picked to show demonstrate the Fourier-leakage effect. Given are the frequencies and the corresponding indices (rounded and exact values) for each pattern. All images are normalized and the exact intensity level (yellow) is given below the pattern.

B. Comparison of Information Loss during Image Scaling

In Fig. B.1 a descriptive example is shown to demonstrate information loss during the proposed scaling processes. While direct scaling loses the exact position of the two sample points, this information can be reconstructed by zero-filling using the Fourier-scaled process.

It seems to be useful to use the Fourier-scaling method for filling the system matrix, because there is higher quality information available. A look at Fig. B.2
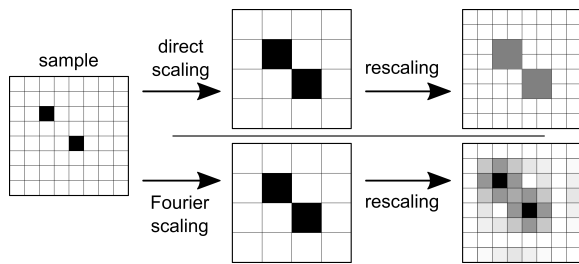
Figure B.1: Example of a two-point phantom and the influence of the scaling process. While the exact position is lost using the direct scaling, it can be reconstructed using the Fourier-scaling and zero-filling.

shows the eigenvalues of a system matrix build with the direct-scaled data and the Fourier-scaled data. These values are calculated during a SVD. The eigenvalues show different distributions: in the case of direct-scaled all eigenvalues are within three orders of magnitude, which yields a good reconstruction capability of 'unknown' pattern.

In contrast, the eigenvalues of Fourier-scaled are much higher at the beginning, but decrease by more than eight orders of magnitude at higher indices. This results in a more robust reconstruction in the presence of noise using truncated SVD.
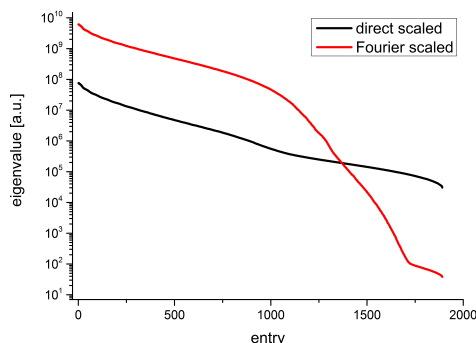

Figure B.2: The graph shows the eigenvalues of the system matrices build with the direct-scaled data and with the Fourier-scaled data.

C. Effect of Patch Selection on Signal Intensity

In the following a more detailed description of the effect of patch selection on the signal intensity in the final reconstructed image is given.

In Fig. C.1 (a) the patch selection and the corresponding reconstructed images are shown. In this case, the sample points lie next to the border of the system matrix
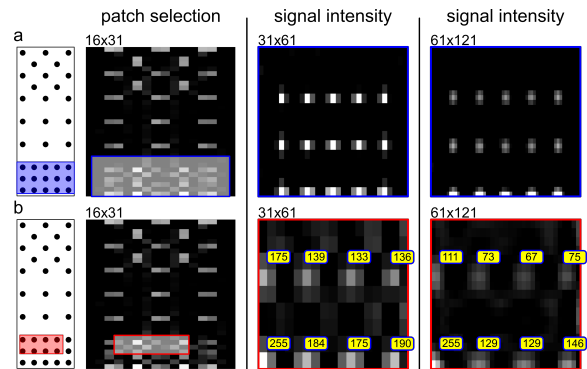

Figure C.1: Different patch selections and the influence on the reconstructed images depending on the grid size: (a) The patch area contains sample points, which lie next to the border of the system matrix. (b) The selected patch contains an area in the center, with some of the sample points lying next to the border.

grid. Thus, the selected patch is also set up to the border. Depending on the grid size, the reconstruction process calculated the intensities of the point samples differently. The effect stems from the influence of signal, which is incorrectly reconstructed for pixels outside the border. Because of the limited grid area, this signal is projected onto the adjacent pixel inside the selected patch, which results in an intensity increase. In Fig. C.1 (b) the same effect is shown with a selected patch area inside the matrix grid, but also cutting through an area of sample points. Again, the samples next to the border show increased intensity, which gets higher with a finer grid. This happens because signal of more pixels is reconstructed, which are lying outside the patch area and the respective intensities are projected onto the pixel next to the border inside the patching area [16].

References

[1] B. Gleich and J. Weizenecker. Tomographic imaging using the nonlinear response of magnetic particles. *Nature*, 435(7046):1214–1217, 2005. doi:10.1038/nature03808.

[2] N. Panagiotopoulos, R. L. Duschka, M. Ahlborg, G. Bringout, C. Debbeler, M. Graeser, C. Kaethner, K. Lüdtke-Buzug, H. Medimagh, J. Stelzner, T. M. Buzug, J. Barkhausen, F. M. Vogt, and J. Haegele. Magnetic particle imaging: current developments and future directions. *Int. Journ. Nanomed.*, 10:3097, 2015. doi:10.2147/IJN.S70488.

[3] J. Weizenecker, B. Gleich, and J. Borgert. Magnetic particle imaging using a field free line. *J. Phys. D: Appl. Phys.*, 41(10):105009, 2008. doi:10.1088/0022-3727/41/10/105009.

[4] J. Rahmer, J. Weizenecker, B. Gleich, and J. Borgert. Signal encoding in magnetic particle imaging: properties of the system function. *BMC Medical Imaging*, 9(4), 2009. doi:10.1186/1471-2342-9-4.

[5] P. W. Goodwill and S. M. Conolly. The x-space formulation of the magnetic particle imaging process: One-dimensional signal, resolution, bandwidth, SNR, SAR, and magnetostimulation. *IEEE Trans. Med. Imag.*, 29(11):1851–1859, 2010. doi:10.1109/TMI.2010.2052284.

[6] P. Vogel, S. Lother, M.A. Ruckert, W.H. Kullmann, P.M. Jakob, F. Fidler, and V.C. Behr. Mri meets mpi: A bimodal mpi-mri tomograph. *IEEE Trans. Med. Imag.*, 33(10):1954–1959, 2014. doi:10.1109/TMI.2014.2327515.

[7] J. J. Konkle, P. W. Goodwill, O. M. Carrasco-Zevallos, and S. M. Conolly. Projection reconstruction magnetic particle imaging. *IEEE Trans. Med. Imag.*, 32(2):338–347, 2012. doi:10.1109/TMI.2012.2227121.

[8] T. Knopp and T. M. Buzug. *Magnetic Particle Imaging: An Introduction to Imaging Principles and Scanner Instrumentation.* Springer, Berlin/Heidelberg, 2012. doi:10.1007/978-3-642-04199-0.

[9] P. Vogel, M. A. Rückert, P. Klauer, W. H. Kullmann, P. M. Jakob, and V. C. Behr. Traveling wave magnetic particle imaging. *IEEE Trans. Med. Imag.*, 33(2):400–407, 2014. doi:10.1109/TMI.2013.2285472.

[10] P. Vogel, M. A. Rückert, P. Klauer, W. H. Kullmann, P. M. Jakob, and V. C. Behr. Rotating slice scanning mode for traveling wave magnetic particle imaging. *IEEE Trans. Magn.*, 51(2):6501503, 2015. doi:10.1109/TMAG.2014.2335255.

[11] P. Vogel, M. A. Rückert, P. Klauer, W. H. Kullmann, P. M. Jakob, and V. C. Behr. First in-vivo traveling wav magnetic particle imaging of a beating mouse heart. *Phys. Med. Biol.*, 61(18):6620–6634, 2016. doi:10.1088/0031-9155/61/18/6620.

[12] T. Knopp, T. F. Sattel, S. Biederer, J. Rahmer, J. Weizenecker, B. Gleich, J. Borgert, and T. M. Buzug. Model-based reconstruction for magnetic particle imaging. *IEEE Trans. Med. Imag.*, 29(1):12–18, 2009. doi:10.1109/TMI.2009.2021612.

[13] M. Schilling, F. Ludwig, C. Kuhlmann, and T. Wawrzik. Magnetic particle imaging scanner with 10-khz drive-field frequency. *Biomed. Tech. / Biomed. Eng.*, 58(6):557–563, 2013. doi:10.1515/bmt-2013-0014.

[14] T. Knopp, J. Rahmer, T. F. Sattel, S. Biederer, J. Weizenecker, B. Gleich, J. Borgert, and T. M. Buzug. Weighted iterative reconstruction for magnetic particle imaging. *Phys. Med. Biol.*, 55(6):1577–1589, 2010. doi:10.1088/0031-9155/55/6/003.

[15] D. Kalman. A singularly valuable decomposition: the svd of a matrix. *College Math. J.*, 27(1):2–23, 1996. doi:10.2307/2687269.

[16] P. C. Hansen. *Rank-Deficient and Discrete Ill-Posed Problems: Numerical Aspects of Linear Inversion.* SIAM, Philadelphia, 1998. doi:10.1137/1.9780898719697.

[17] P. Vogel, M. A. Rückert, and V. C. Behr. 3D-GUI simulation environment for MPI. In *International Workshop on Magnetic Particle Imaging (IWMPI)*, 2016.

[18] J. A. Parker, R. V. Kenyon, and D. E. Troxel. Comparison of interpolating methods for image resampling. *IEEE Trans. Med. Imag.*, 2(1):31–39, 1983. doi:10.1109/TMI.1983.4307610.

[19] G. H. Golub and C. F. Van Loan. *Matrix Computations.* Hopkins University Press, Baltimore, 1996.

[20] A. Weber, F. Werner, J. Weizenecker, T. M. Buzug, and T. Knopp. Artifact free reconstruction with the system matrix approach by overscanning the field-free-point trajectory in magnetic particle imaging. *Phys. Med. Biol.*, 61(2):475–487, 2016. doi:10.1088/0031-9155/61/2/475.

[21] P. Vogel, M. A. Rückert, S. J. Kemp, A. P. Khandhar, R. M. Ferguson, A. Vilter, P. Klauer, K. M. Krishnan, and V. C. Behr. Micro traveling wave MPI – initial results with optimized tracer LS-008. In *International Workshop on Magnetic Particle Imaging (IWMPI)*, 2016.

[22] W. H. Press, S. A. Teukolsky, W. T. Vetterling, and B. P. Flannery. *Numerical Recipes.* Cambridge University Press, Cambridge, 2007.